Determining the soil-water retention curve using mercury intrusion porosimetry test in consideration of soil volume change

Wen-Jing Sun, Yu-Jun Cui

Determination of soil water retention curve by mercury intrusion porosimetry tests with consideration of soil volume change

Wen-Jing Sun[1], Yu-Jun Cui[2]

1: State Key Laboratory of Geomechanics and Geotechnical Engineering, Institute of Rock and Soil Mechanics, Chinese Academy of Sciences, Wuhan 430071, China
Department of Civil Engineering, Shanghai University, Shanghai 200444, P. R. China

2: Ecole des Ponts ParisTech, Laboratoire Navier/CERMES, 6 – 8 avenue Blaise Pascal, Cité Descartes, Champs – sur – Marne, 77455 Marne – la – Vallée cedex 2, France
Institute for the Conservation of Cultural Heritage, Shanghai 200444, P. R. China
Email: wjsun@shu.edu.cn
Phone: +86 21 66135783
Fax: +86 21 66133698

Yu-Jun Cui
Corresponding author
Ecole des Ponts ParisTech, Laboratoire Navier/CERMES, 6 – 8 avenue Blaise Pascal, Cité Descartes, Champs – sur – Marne, 77455 Marne – la – Vallée cedex 2, France.
Email : yujun.cui@enpc.fr
Phone : +33 1 64 15 35 50
Fax : +33 1 64 15 35 62

Abstract:

There is close link between soil water retention curve and pore size distribution. Theoretically, mercury intrusion porosimetry (MIP) test simulates a soil drying path and the soil water retention curve $SWRC_{MIP}$ can be deduced from the MIP results. However, $SWRC_{MIP}$ does not include the volume change effect, as opposed to the conventional SWRC which is directly determined by suction measurement or suction control techniques. Therefore, for deformable soils, there is significant difference between SWRC and $SWRC_{MIP}$. In this study, drying test was carried out on a reconstituted silty soil, and the volume change, suction and pore size distribution (PSD) were determined on samples at different water contents. The change of the deduced $SWRC_{MIP}$ and its relation with the conventional SWRC were analyzed, showing that the volume change of soil is the main reason for the difference between the conventional SWRC and the $SWRC_{MIP}$. Furthermore, based on the test results, a transformation model was proposed for SWRC and $SWRC_{MIP}$, by taking the soil state with no longer volume change as a reference. Comparison between the experimental and predicted SWRCs showed that the proposed model can satisfactorily consider the influence of soil volume change on its water retention property.

Key words: Soil-water retention curve; mercury intrusion porosimetry; transform; S_r-*s*-*e* plot; deformable soils

1. INTRODUCTION

A soil-water retention curve (SWRC) describes the amount of soil water (in terms of gravimetric water content w or volumetric water content ϑ or degree of saturation S_r) at a given suction s. This curve is essential in analysing water transfer in unsaturated soils. This curve is also of paramount importance when modelling the coupled hydro-mechanical behaviour of unsaturated soils (Wheeler, 1996; Sun et al., 2007; Nuth and Laloui, 2008; Sun and Sun, 2012).

Conventional SWRC are usually investigated using either suction measurement or suction control techniques. However, application of these techniques is usually time consuming (Aubertin et al., 2003), especially for clayey soils. As volume change can occur when changing suction, the conventional SWRC includes the effect of this volume change. There are numerous SWRC models available in the literature, such as Brooks and Corey model (Brooks and Corey, 1964), van Genuchten model (Van Genuchten, 1980) and Fredlund and Xing model (Fredlund and Xing, 1994), to name only a few. But these models do not account for the volume change effect. Fredlund (2018) proposed mathematical algorithms combining the shrinkage curve and the SWRC, allowing for the separation of volume change effect from the effect of degree of saturation.

Based on the pore size distribution (PSD) obtained from mercury intrusion porosimetry (MIP) test, the soil water retention curve in the drying path can be obtained by applying Laplace's equation (Prapaharan et al., 1985; Delage et al., 1995;

Romero et al., 1999; Aung et al., 2001; Simms and Yanful, 2002, 2005; Muñoz-Castelblanco et al., 2012; Hu et al., 2013). It is worth noting that the SWRC derived by MIP result represents the SWRC under constant void ratio, which is termed as $SWRC_{MIP}$. Accordingly, the derived degree of saturation and suction relationship is termed as S_{rMIP}-s, the derived water content and suction relationship as w_{MIP}-s and the derived void ratio and suction relationship as e_{MIP}-s.

Delage et al. (1995) analysed the PSDs and the SWRCs of various geomaterials, i.e., a siliceous and a clayey sandstone, an overconsolidated clay and a compacted silt. A good agreement was observed between $SWRC_{MIP}$ and SWRC for sandstones, while this agreement was not observed for fine-grained soils. Muñoz-Castelblanco et al. (2012) also reported a significant difference between $SWRC_{MIP}$ and SWRC for a loess. These differences were discussed in the literature, but no conclusive explanations were given. For example, Romero et al. (1999) thought that the differences could arise from the different effects that water and dissolved salts produce on clay fabric compared to the process in mercury intrusion. While Simms and Yanful (2002) mentioned the possible pore trapping effect; that is, mercury intrusion only gives the entrance pore radius, thus somewhat overestimating the porous volume associated with the estimated diameter.

Normally, soil microstructure is sensitive to changes in water content, especially for deformable soils. Delage et al. (1995) concluded that soil water retention properties were conditioned by the microstructure changes. Muñoz-Castelblanco et al. (2012) also showed the significant effects of changes in microstructure occurring at the level

of clay aggregations and the growing importance of the water adsorption in the clay fraction at high suctions. The hydraulic and mechanical responses of soil take place simultaneously when it is subjected to suction changes. That is to say, the total change in degree of saturation is induced by both changes in suction and void ratio (Simms and Yanful, 2005; Mašín, 2010; Romero et al., 2011; Sun and Sun, 2012; Hu et al., 2013; Sun et al., 2014; Della Vecchia et al., 2015; Vaunat and Casini, 2017; Fredlund, 2018). Therefore, it can be deduced that microstructural changes may be the reason for the difference between the conventional SWRC and $SWRC_{MIP}$, especially for deformable soils.

Recently, the coupled hydro-mechanical response due to suction changes was accounted for by several authors (Gallipoli et al., 2003; Simms and Yanful, 2005; Sun et al., 2007; Nuth and Laloui, 2008; Mašín, 2010; Hu et al., 2013; Tsiampousi et al., 2013; Fredlund, 2018). Some of them proposed the approach based on the quantitative information derived from MIP data. Simms and Yanful (2005) developed a deformable pore-network model (DPNM) to predict the SWRC based on the evolution of measured PSDs for a compacted clayey soil under isotropic loading and/or desaturation. While in the DPNM model, pores are randomly mapped in space and idealized as a network. Hu et al. (2013) formulated a hysteretic SWRC model to account for the influence of deformation on the variation of saturation based on the changes in PSD function for deformable soils. In their model, the PSD at a deformed state can be obtained by horizontal shifting and vertical scaling of the PSD function from a reference state - initial state with void ratio e_0. The premise of the model is that the overall shapes of the various PSDs can be considered to be insignificantly different

from each other. This is obviously too strong hypothesis for fine-grained soils as illustrated by Sun and Cui (2018), testifying that the changes in the aggregate porosity were not negligible. Romero et al. (2011) and Della Vecchia et al. (2015) proposed a physically based conceptual framework for modelling the retention behaviour of compacted clayey soils, which considers the PSD function evolution along hydraulic and mechanical paths. However, their framework contains a large number of parameters to be calibrated, limiting its application.

In this paper, drying tests were conducted on a reconstituted silty soil. The volume, suction and PSD were determined on samples at different target water contents. Based on the obtained results, the difference between the conventional SWRC and the $SWRC_{MIP}$ derived from PSD was analysed. Particular attention was paid to the interrelationship between the $SWRC_{MIP}$ families and the conventional SWRC. Moreover, a transformation model was established between SWRC and $SWRC_{MIP}$, allowing the prediction of SWRC from the $SWRC_{MIP}$ families. Through this study, the water retention mechanism associated with the volume change of soil was clearly evidenced.

2. MATERAIL, TESTING PROGRAM AND CALCULATING METHOD

2.1 Material and testing program

An aeolian Jossigny silt was used. The liquid limit w_l is 37%, the plastic limit w_p is 19% and the shrinkage limit w_s is 12%. In the Casagrande diagram of plasticity, the soil is

140 located close to the A-line, belonging to low plasticity clay. The clay-size fraction of
141 Jossigny silt is 34 %.
142
143 Soil slurry, with a water content 1.5 times the liquid limit mixed with deionised water,
144 was firstly poured into several small containers. Afterwards, the samples in the
145 containers were air-dried to different target water contents, which were selected
146 around w_l, w_p and w_s. The air-drying intervals were taken short - every 30 minutes - to
147 avoid macro-cracks in samples. After each drying operation, the container was
148 covered for several hours for water homogenisation. By repeating these steps, dried
149 samples at different water contents were obtained.
150
151 After reaching the respective target water content, the sample was divided into 4
152 pieces. One for water content measurement. A second for the volume measurement
153 based on the principle of buoyancy (Delage et al., 2007; Zeng et al., 2017). A third was
154 freeze-dried for MIP investigation (Delage and Lefebvre, 1984; Delage et al., 1996)
155 using an Autopore IV 9500 mercury intrusion porosimeter (Micrometrics), which
156 operated from 3.4 kPa (363.6 µm pore) to 227.5 MPa pressure (5.5 nm pore). The last
157 one was used for suction measurement using a chilled-mirror dew-point
158 psychrometer (WP4C Dewpoint PotentiaMeter). To measure low suction of soil, a test
159 apparatus consisting of an odometer cell with 70 mm inner diameter, a porous
160 ceramic disc with an air-entry pressure of 50 kPa and a graduated tube with 6 mm
161 inner diameter connected to a water tank was used. More details about this apparatus
162 can be found in Feia et al. (2014) and Sun et al. (2017). Table 1 shows the indexes of
163 samples dried to different target states.

164

165 *2.2 Calculating method*

166

167 The mercury intrusion process is assimilated to a drying process, in which a non-
168 wetting liquid is penetrating into a porous medium full of wetting fluid (Delage et al.,
169 1996; Muñoz-Castelblanco et al., 2012).

170

171 The pore diameter can be deduced from the mercury pressure, as follows (Romero et
172 al., 1999):

173 $$d = -\frac{4T_m \cos\theta_m}{p} \quad (1)$$

174 where T_m is the surface tension of mercury (0.485N/m); d is the pore entrance
175 diameter (μm); ϑ_m is the mercury-soil contact angle (taken equal to 130° in this study);
176 p is the external applied intrusion pressure ($\times 10^6$ N/m^2).

177

178 The cumulative intrusion void ratio (e_{MIP}) is computed as follows:

179 $$e_{MIP} = \frac{V_m}{V_s} = \frac{V_m}{m_s} \cdot G_s \cdot \rho_w \quad (2)$$

180 where V_s is the volume of soil; V_m is the volume of intruded mercury; m_s is the mass of
181 soil; G_s is the specific gravity; ρ_w is the water unit mass.

182

183 From the derivative of the cumulative intrusion curve, the pore size density function
184 is obtained:

185 $$f = -\frac{\delta(e_{MIP})}{\delta(\lg d)} \quad (3)$$

Based on the PSD obtained from MIP test, the $SWRC_{MIP}$ can be determined (Prapaharan et al., 1985; Romero et al., 1999; Aung et al., 2001; Simms and Yanful, 2002). The relationship between matric suction (u_a - u_w) and mercury intrusion pressure p can be deduced from Eq. (4):

$$u_a - u_w = -\frac{T_w \cos\theta_w}{T_m \cos\theta_m} p \tag{4}$$

where T_w is the surface tension of water (0.073N/m); ϑ_w is the water-soil contact angle (taken equal to 0° in this study).

Romero et al. (1999) suggested that the degree of saturation S_r and water content w corresponding to the equivalent applied pressure should consider the hygroscopic water content related to the strongly attracted adsorbed water to the mineral surface and the equivalent residual water content corresponding to the non-intruded porosity. They can be expressed as follows:

$$S_r = (1 - S_{rm}) + \frac{w_{\text{res}}}{w_{\text{sat}}} S_{rm} \tag{5}$$

$$w = (1 - S_{\text{rm}})(w_{\text{sat}} - w_{\text{res}}) + w_{\text{res}} \tag{6}$$

where w_{sat} stands for the saturated gravimetric water content; S_{rm} stands for the non-wetting mercury degree of saturation; w_{res} is the equivalent residual water content corresponding to the maximum mercury intrusion pressure that the mercury porosimeter can reach.

S_{rm} and w_{res} can be calculated as follows:

$$S_{rm} = \frac{V_m}{V_{m\max}} = \frac{e_{MIP}}{e_{MIPmax}} \quad (7)$$

$$w_{\text{res}} = \frac{\mathrm{m}_{w\text{res}}}{m_s} = \frac{\rho_w \left(V_v - V_{m\max}\right)}{m_s} = \frac{e - e_{MIP\max}}{G_s} \quad (8)$$

Finally,

$$w_{MIP} = \frac{e}{G_s}\left(1 - \frac{e_{MIP}}{e}\right) \quad (9)$$

$$S_{rMIP} = 1 - \frac{e_{MIP}}{e} \quad (10)$$

where e_{MIP} is the mercury intruded void ratio; e_{MIPmax} is the maximum mercury intruded void ratio; e is the void ratio corresponding to different target drying states; S_{rMIP} is the degree of saturation obtained from MIP test; w_{MIP} is the water content derived from MIP test.

Based on the above measurements and calculations, the void ratios and degrees of saturation of soil samples at different target water contents were calculated, and the conventional SWRC and the $SWRC_{MIP}$ derived from PSD were also determined.

3 EXPERIMENTAL RESULTS

3.1 Shrinkage behaviour and conventional SWRC

Figure 1 shows the results from the drying tests on the reconstituted Jossigny silt prepared at initial water content w_i = 1.5 w_l. Figs. 1 (a) and (c) depict the shrinkage

behaviour, e.g., the changes of void ratio with water content (e - w), and degree of saturation with water content (S_r - w), respectively. Fig. 1(b) depicts the volume change behaviour under the effect of suction, e.g., void ratio with suction (e-s). Figs. 1(d) shows the conventional S_r-SWRC of Jossigny silt.

The e-w relationship obeys a typical shrinkage characteristic curve of soils, as shown in Fig. 1(a), which includes normal shrinkage, residual shrinkage and no shrinkage stages. The experimental results firstly started from the stage of normal shrinkage, which coincided with the dashed full saturation line, and the samples kept fully saturated, as shown in Fig. 1(c) for the S_r-w relationship. Afterwards, when water content reached w_{ae}, the slope of the shrinkage curve decreased, and the residual shrinkage began. From the air entry point, the degree of saturation began to decline, as it can be seen from the S_r-w curve in Fig. 1(c). From the S_r-SWRC in Fig. 1(d), the corresponding suction at w_{ae} could be determined of about 180 kPa. When suction s exceeded the air entry value, S_r-SWRC changed from the saturated to the unsaturated domain. After the water content reached the shrinkage limit w_s, the void ratio remained unchanged with further drying, as shown in Fig. 1(a) and (b), starting the no shrinkage stage.

3.2 Microstructure investigation

Figure 2 presents the pore size distribution of Jossigny silt during drying. Fig. 2(a) is the cumulative intruded curves. It can be observed that e_{MIP} decreased in the beginning and became almost unchanged after the water content reached the shrinkage limit. The pore size density functions shown in Fig. 2(b) are the derivative of the cumulative

intrusion curves of No. (1)-(6) in Fig. 2(a), plotted in terms of $\delta e_{MIP}/\delta \lg d$ as a function of pore entrance diameter d. From Fig. 2(b), all the PSD curves present a typical unimodal pattern (Fiès and Bruand, 1998). When $w>w_s$, significant pore refinement occurred upon drying. However, with further drying, the curves began shifting to larger diameter. Sun and Cui (2018) explained this phenomenon by the development of possible micro-fissures of the clay part. Moreover, when $w<w_s$, the shift trend of PSD curves ceased. Accordingly, the void ratio at this time almost remained unchanged and reached the minimum value, e_{min}.

3.3 $SWRC_{MIP}$ derived from MIP investigations

Figure 3 presents the relationship between degree of saturation and suction. The plots star (✯) show the conventional SWRC results determined directly by suction measurement, the others corresponding to the samples with different target water contents. It can be noticed that the $SWRC_{MIP}$ significantly differs from the conventional SWRC.

$SWRC_{MIP}$ can be divided into three segments on a semi-logarithmic plot, that is, a boundary effect zone, a transition zone and a residual zone:

(i) In the boundary effect zone, S_{rMIP} was almost equal to 100%, where almost no mercury intrusion took place.

(ii) In the transition zone, sudden drops occurred because of the intrusion of the dominant pore diameters. It was also observed that the S_{rMIP}-s curve shifted towards the S_r-s curve at the beginning, however in the residual shrinkage stage, the S_{rMIP}-s curve began to shift backwards due to the possible presence of drying-induced internal micro-fissures occurred in the clay fractions and in the interface between silt grain and clay particles, more details can be found in Sun and Cui (2018).

(iii) In the residual zone, the S_{rMIP}-s curves showed a shifting-up with further drying, and got close to the S_r-s curve. The S_{rMIP} represents the volume fraction of the non-intruded space and can be expressed as $S_{rMIP}=(e-e_{MIP})/e$ in Eq.(10). The shifting-up of the S_{rMIP}-s curve in the residual zone was the result of the changes of non-intruded void ratio (e-e_{MIP}). The changes of S_{rMIP}-s curves were also related to the microstructure change during drying. Moreover, it could be deduced according to the shifting-up trend that the S_{rMIP}-s curve of sample with the smallest void ratio ($e=e_{min}$) almost reached the S_r-s curve. At this time, the $SWRC_{MIP}$ from MIP test is the same as the conventional SWRC, in agreement with the observation of Delage et al. (1995).

3.4 S_r-s & S_{rMIP}-s relationships

Figure 4 shows the sketch of S_r-s relationship (solid line from A to B) and S_{rMIP}-s relationship (dash line from A to C). Point A marks the coordinate (S_{ri}, s_i) with void ratio e_i and water content w_i, and Point B (S_{ri+1}, s_{i+1}) with void ratio e_{i+1} and water content w_{i+1}. From A to B, when the suction increased from s_i to s_{i+1}, the degree of saturation

298 decreased from S_{ri} to S_{ri+1}. The absolute change value in degree of saturation when
299 suction increased from s_i to s_{i+1} is $|\mathrm{d}S_r| = |S_{ri+1} - S_{ri}|$.
300
301 The change in degree of saturation at constant void ratio e_i when suction increased
302 from s_i to s_{i+1} followed the S_{rMIP}-s curve from A to C, and could be described as $|\mathrm{d}S_r(s)_{e=ei}|$, which could be obtained by the S_{rMIP}-s curve at constant void ratio e_i, i.e., $\mathrm{d}S_r(s)_{e=ei} = \mathrm{d}S_{rMIP\,e=ei}$.
305
306 Therefore, the change in degree of saturation caused by void ratio change under a
307 constant suction ($s = s_i$) could be determined as $|\mathrm{d}S_r(e)_{s=si}|$, and it could be calculated
308 by $|\mathrm{d}S_r(e)_{s=si}| = |\mathrm{d}S_r(s)_{e=ei}| - |\mathrm{d}S_r|$.
309
310 From the drying tests, the relationships between degree of saturation and suction (S_r-
311 s) and between void ratio and suction (e-s) were obtained. Combined with the MIP
312 results, the changes of $|\mathrm{d}S_r(e)| / |\mathrm{d}S_r(s)|$ and $|\mathrm{d}S_r| / |\mathrm{d}S_r(s)|$ with suction were
313 determined, as shwon in Fig. 5. It can be seen from the changes in $|\mathrm{d}S_r(e)| / |\mathrm{d}S_r(s)|$
314 (dash line) that with increasing suction, the value changes from 1 to 0 gradually,
315 indicating that when suction is low, the reduction of degree of saturation is mainly
316 caused by the changes of void ratio. By contrast, when the water content reached the
317 shrinkage limit, the void ratio kept almost unchanged, and the contribution of void
318 ratio to the change of degree of saturation $|\mathrm{d}S_r|$ vanished. Conversely, with
319 increasing suction, the value $|\mathrm{d}S_r| / |\mathrm{d}S_r(s)|$ changed from 0 to 1 gradually, indicating
320 that when suction was low, the degree of saturation almost kept 100%. At higher

suction, the void ratio tended to become unchanged and the change of degree of saturation was totally caused by suction change, that is, $|dS_r| = |dS_r(s)|$.

For non-deformable soils, the S_{rMIP}-s curves are consistent with the S_r-s curve (Delage et al., 1995), the value $|dS_r| / |dS_r(s)|$ can be approximately taken equal to 1. On the contrary, for deformable soils, the shapes of S_{rMIP}-s curve and S_r-s curve differ significantly and the value $|d S_r| / |d S_r(s)|$ changes from 0 to 1 gradually with the increase of suction.

3.5 S_r-e-s & S_{rMIP}-e-s three-dimension surfaces

In order to better visualise the effect of void ratio on SWRC, two diagrams are proposed: one is the S_r-e-s three-dimension diagram and another is the S_{rMIP}-e-s three-dimension diagram, as shown in Fig. 6. The conventional SWRC is located on the S_r-e-s 3D surface with void ratio changing, while the $SWRC_{MIP}$ with constant void ratio is located on the S_{rMIP}-e-s 3D surface.

The F-X equation (Fredlund and Xing, 1994), with the applied correction factor for zero water content at 10^6 kPa of suction, was adopted in building the three-dimension surface for further investigation, as shown in equation (11). However, it is worth noting that other suitable models can be also used provided that they allow the description of the data over the full suction range.

$$S_r = \left(1 - \frac{\ln(1 + s / s_{res})}{\ln(1 + 10^6 / s_{res})}\right)\left[\frac{1}{\ln(2.718 + (s / a)^n}\right]^m \quad (11)$$

where s is suction; s_{res} is the suction corresponding to the equivalent residual water content; parameters a, n, and m affect the shape of the curve.

The S_{rMIP}-e-s three-dimension surface can be obtained by the following method: first, the S_{rMIP}-s curve at constant void ratio e = e_i was derived from the PSD curve obtained from MIP test. Second, each S_{rMIP}-s (e = e_i) relationship was expressed through the F-X SWRC model, namely formula (11), each curve having its corresponding three parameters $a(e_i)$, $n(e_i)$, $m(e_i)$. Thus, the function of the parameter changing with the void ratio could be determined. Finally, the S_{rMIP}-e-s three-dimension surface was built.

From the w-s relationship matched by the F-X SWRC model and the equation $e\ S_r = G_s\ w$, the S_r-e-s surface was obtained. After that, several SWRCs at constant void ratio were obtained through the F-X SWRC model.

Figure 7 shows the projection of drying test results in S_r (S_{rMIP})-e-s diagram, the thick solid curve is the conventional SWRC in drying path obtained in this study, and the thick dash curve is the SWRC projection on the S_{rMIP}-e-s surface. The projections of the two thick curves onto S_r (S_{rMIP})-o-s, S_r (S_{rMIP})-o-e, and e-o-s surfaces are also shown. It is worth noting that, in S_r-o-s coordinate, the projection of the thick solid curve is conventional S_r-s relationship in drying path, with void ratio changing following the projection in e-o-s coordinate.

The projection of drying test results on e-o-s coordinate is shown in Fig.1(b). It can be observed that the void ratio decreased with increasing suction. Figure 8 shows the

368 sketch of *e*-*s* relationship corresponding to the drying test result. It can be seen that
369 each suction s_i had a corresponding relationship with the void ratio e_i. Combing the
370 test results in Fig.1(b) and the sketch of *e*-*s* relationship in Fig.8, it is observed that the
371 water content reached the shrinkage limit at w_s=12%, corresponding to suction s_s
372 =1500 kPa and void ratio is e_s=0.52. Under further drying, the void ratio remained
373 almost unchanged. When suction reached 10^6 kPa, the void ratio reached the
374 minimum value: $e=e_{min}$ (about 0.49).
375
376 Figure 9 shows the projection of the test results on S_r (S_{rMIP})-*o*-*s* coordinate. The plots
377 star (✯) show the conventional SWRC results obtained in this study. Correspondingly,
378 the thick solid curve represents the conventional S_r-*s* relationship. The dash dot curve
379 represents the S_{rMIP}-*s* ($e=e_i$) curve, which can be regarded as one of the MIP test results
380 in the study, or as one of the curves selected from the S_{rMIP}-*e*-*s* surface at any void
381 ratio e_i. It is to be mentioned that the corresponding S_{rMIP}-*s* ($e=e_{min}$) curve, represented
382 by a dash curve, was obtained from the established S_{rMIP}-*e*-*s* three-dimension surface
383 at $e=e_{min}$.
384
385 As observed previously, the S_{rMIP}-*s* curve moved rightwards with void ratio decreasing
386 under the premise that there are no micro-fissures developed during drying. After the
387 water content reached the shrinkage limit, the void ratio approached the minimum
388 value e_{min} gradually. It can be reasonably assumed that the S_r-*s* ($e=e_{min}$) curve in S_r-*e*-*s*
389 3D surface, the S_{rMIP}-s ($e=e_{min}$) relationship in S_{rMIP}-*e*-*s* 3D surface and the projection
390 of the conventional S_r-SWRC on S_r-o-*s* coordinate coincide in the high suction range.
391 This is testified in Fig. 9. Therefore, the S_{rMIP}-s ($e=e_{min}$) curve can be taken as the

reference curve, which connects the two surfaces, S_{rMIP}-e-s and S_r-e-s.

4. TRANSFORMATION FROM S_{rMIP}-s CURVES TO CONVENTIONAL S_r-s RELATIONSHIP

From above analysis, it is noticed that a $SWRC_{MIP}$ corresponds to a fixed pore structure, however, a real SWRC is affected by soil volume changes. It can also be deduced that S_{rMIP}-s curves would move continuously toward the S_r-s curve under the condition of no micro-fissures occurring, i.e., theoretically, a SWRC is the combination of a family of $SWRC_{MIP}$s at different suctions. Based on the finding that the S_{rMIP}-s (e=e_{min}) curve can be taken as a reference curve, connecting the S_{rMIP}-e-s and the S_r-e-s surfaces, a transformation model was established to predict the SWRC from the $SWRC_{MIP}$ families, accounting for the effect of soil volume change on soil water retention property.

4.1 Transformation model

As the conventional S_r-SWRC coincides with the S_{rMIP}-s curve at e=e_{min}, as shown in Fig. 9, namely $S_r(s=s_i,\ e=e_i)$ = $S_{rMIP}(s=s_i,\ e=e_{min})$, the difference between S_r on the S_r-e-s surface and S_{rMIP} on the S_{rMIP}-e-s surface when s=s_i, combined with Eq.(10), can be expressed as:

$$S_r\left(s=s_i,e=e_i\right)-S_{rMIP}\left(s=s_i,e=e_i\right) \tag{13}$$

$$=S_{rMIP}\left(s=s_i,e=e_{\min}\right)-S_{rMIP}\left(s=s_i,e=e_i\right)$$

$$=1-\frac{e_{MIP}\left(s=s_i,e=e_{\min}\right)}{e_{\min}}-1+\frac{e_{MIP}\left(s=s_i,e=e_i\right)}{e_i}$$

414 $$= \frac{e_{MIP}\left(s=s_i, e=e_i\right)}{e_i} - \frac{e_{MIP}\left(s=s_i, e=e_{\min}\right)}{e_{\min}}$$

415 where $e_{MIP}(s=s_i, e=e_i)$ represents the amount of mercury intrusion for soil sample with
416 void ratio equals e_i, and with pore diameter $d \geqslant d_i$ and corresponding $s \leqslant s_i$. Figure 10
417 shows the e_{MIP}-s relationship, the solid curve represents the condition of $e=e_i$, $e_{MIP}(s=s_i,$
418 $e=e_i)$ is namely the mercury intrusion porosity ratio when $e=e_i$, $s \leqslant s_i$ and $d \geqslant d_i$, and the
419 dash curve represents the condition of $e=e_{min}$, $e_{MIP}(s=s_i, e=e_{min})$ is namely the mercury
420 intrusion porosity ratio when $e=e_{min}$, $s \leqslant s_i$ and $d \geqslant d_i$.

421

422 Figure 11 shows the pore size distribution diagram, which shows the change of PSD
423 function when e decreases from e_i to e_{min}. $e_{MIP}(s=s_i, e=e_i)$ and $e_{MIP}(s=s_i, e=e_{min})$ can be
424 expressed as:

425 $$\begin{aligned} e_{MIP}\left(s=s_i, e=e_i\right) &= A_{d\geq d_i}(e=e_i)\cdot e_i \\ e_{MIP}\left(s=s_i, e=e_{\min}\right) &= A_{d\geq d_i}(e=e_{\min})\cdot e_{\min} \end{aligned} \quad (14)$$

426 where $A_{d\geq di}(e=e_i)$ represents the porosity proportion of $d \geq d_i$, which is the proportion
427 of the shaded area with cross grain on the PSD curve of $e=e_i$, and $A_{d \geqslant di}$ $(e=e_{min})$
428 represents the porosity proportion of $d \geqslant d_i$, which is the proportion of the shaded
429 area with vertical stripe on the PSD curve of $e=e_{min}$. When the void ratio decreases to
430 e_{i+n}, the pore entrance diameter decreases to d_{i+n}, and the corresponding suction
431 increases to s_{i+n}, and $e_{MIP}(s=s_{i+n}, e=e_{i+n})$ and $e_{MIP}(s=s_{i+n}, e=e_{min})$ can be obtained by the
432 above method, combined with Fig.11.

433

434 Therefore, the difference (S_r - S_{rMIP}) at $s=s_i$, in Eq.(13), can be further expressed as:

$$S_r\left(s=s_i, e=e_i\right)-S_{rMIP}\left(s=s_i, e=e_{\mathrm{i}}\right)=A_{d\geq d_i}\left(e=e_i\right)-A_{d\geq d_i}\left(e=e_{\min}\right) \quad (15)$$

It appears from Fig. 6 that the variation between S_r and S_{rMIP}, i.e., (S_r - S_{rMIP}) at $s=s_i$, which is simplified as Y_i, represents the distance between Point A on S_r-e-s 3D surface and Point A_M on S_{rMIP}-e-s 3D surface. When $s=s_{i+1}$, the variation between S_r and S_{rMIP} at $s= s_{i+1}$, simplified as Y_{i+1}, represents the distance between Point B on S_r-e-s 3D surface and Point B_M on S_{rMIP}-e-s 3D surface.

The variation between Y_{i+1} and Y_i, e.g., $\triangle Y$ represents the change of the value (S_r - S_{rMIP}) from point $s=s_i$ to point $s=s_{i+1}$. It can be expressed as:

$$\Delta Y=Y_{i+1}-Y_i \quad (16)$$

$$=\left(S_r-S_{rMIP}\right)_{\left(s=s_{i+1}, e=e_{i+1}\right)}-\left(S_r-S_{rMIP}\right)_{\left(s=s_i, e=e_i\right)}$$

$$=\left(A_{s\leq s_{i+1}}\left(e=e_{i+1}\right)-A_{s\leq s_{i+1}}\left(e=e_{\min}\right)\right)-\left(A_{s\leq s_{\mathrm{i}}}\left(e=e_i\right)-A_{s\leq s_{\mathrm{i}}}\left(e=e_{\min}\right)\right)$$

To summarize, according to Eq.(16), $\triangle Y$ can be obtained by the following steps:

First, the S_{rMIP}-e-s surface can be obtained from at least three MIP experiment results of samples with different void ratios. Second, the S_{rMIP}-s relationship for any void ratio e_i and the minimum void ratio e_{min} can be obtained from the deduced S_{rMIP}-e-s surface. Then, the relationships of e_{MIP}-s at $e=e_i$ and $e=e_{min}$ can be back deduced by the obtained S_{rMIP}-s relationship. The proportional "A" value in Eq.(16) can be obtained from the e_{MIP}-s curves of $e=e_i$ and $e=e_{min}$ or their pore size distribution curves. Finally, the variation Y_i between S_r and S_{rMIP} at $s=s_i$ in Eq.(15) can be obtained. Given the suction increasing step, and the suction reaches $s=s_{i+1}$, by repeating the above procedures, Y_{i+1} between S_r and S_{rMIP} at $s= s_{i+1}$ can also be obtained.

458

459 Simultaneously, from Fig. 6, $\triangle Y$ can also be expressed geometrically as:

460 $$\Delta Y = (S_{r_{i+1}} - S_{rMIP_{i+1}}) - (S_{r_i} - S_{rMIP_i}) = S_{r_{i+1}} - S_{r_i} - (S_{rMIP_{i+1}} - S_{rMIP_i}) \quad (17)$$

461 where $S_{rMIPi+1} - S_{rMIPi} = \triangle S_{rMIP(i+1)-(i)}$ corresponds to the variation of degree of saturation

462 on the S_{rMIP}-e-s three-dimension surface, and includes two parts: one caused by

463 changes of suction and the other caused by changes of void ratio, which can be

464 expressed by the following integral:

465 $$dS_{rMIP}(s_i \to s_{i+1}, e_i \to e_{i+1}) = \frac{\partial S_{rMIP}}{\partial e} de + \frac{\partial S_{rMIP}}{\partial s} ds \quad (18)$$

466

467 Finally, using the values of the degree of saturation and water content at suction s_i,

468 combining Eqs. (16)-(18), the S_{ri+1} and w_{i+1} at s_{i+1} can be deduced, as follows:

469 $$S_{r_{i+1}} = Y_{i+1} - Y_i + S_{r_i} + \Delta S_{rMIP(i+1)-(i)} \quad (19)$$

470 $$w_{i+1} = \frac{e_{i+1} \cdot S_{r_{i+1}}}{G_s} \quad (20)$$

471 Subsequently, the conventional SWRC is predicted from the $SWRC_{MIP}$ families

472 according to the transformation model.

473

474 In summary, in the transformation model, the S_r-e-s three-dimension surface where

475 conventional SWRC is located and S_{rMIP}-e-s three-dimension surface where the

476 $SWRC_{MIP}$ with void ratio unchanging is located were defined. Based on the finding that

477 the S_r-s (e=e_{min}) curve, the S_{rMIP}-s (e=e_{min}) relationship and the conventional S_r-SWRC

478 coincide at high suction, the soil state with no longer volume change is taken as a

479 reference, that is, S_{rMIP}-s (e=e_{min}) curve, which connects the two surfaces, S_{rMIP}-e-s and

480 S_r-e-s. After that, based on the evolution of PSD curves due to the porosity changes,
481 and the variation of S_{rMIP} deduced from the S_{rMIP}-e-s three-dimension surface, the
482 degree of saturation can be determined. Finally, the conventional S_r-SWRC is obtained.
483 It is worth noting that the transformation model introduces no more parameters than
484 those in the F-X model.
485
486 The transformation model is suitable for saturated samples undergoing drying test, no
487 matter what stress histories they have before saturation. Upon wetting, the S_{rMIP}-s
488 curve would shift leftwards due to soil swelling (increase of porosity). Theoretically,
489 the same philosophy of analysis can be applied. This is to be verified later when
490 experimental data are available.
491
492 *4.2 Application of the transformation model*
493
494 Applying the proposed approach, the transformation was completed from the
495 $SWRC_{MIP}$ families to the conventional SWRC. Fig. 12 shows the comparison between
496 the experimental and predicted SWRC from the $SWRC_{MIP}$ families of reconstituted
497 Jossigny silt in drying, including S_r-s relationship in Fig. 12(a) and w-s relationship in
498 Fig. 12(b).
499
500 According to the shrinkage curve of reconstituted Jossigny silt, the minimum void ratio
501 e_{min} is 0.49. In Fig. 12(a), the marks of "✯" shows the SWRC test results; the solid curve
502 represents the predicted S_r-s relationship curve by the transformation model; the
503 marks "□" represents the S_{rMIP}-s relationship, which is obtained as follows: given the

suction increasing step, the corresponding void ratio is obtained by the *e*-*s* curve, and each point in *e*-*s* curve corresponds to a point on the obtained S_{rMIP}-*e*-*s* surface. Then, these points are projected on the S_r (S_{rMIP})-o-*s* coordinate, and the S_{rMIP}-*s* relationship can be obtained.

It can be seen that the S_r-*s* and the *w*-*s* relationship curves predicted by the transformation model are in good agreement with the measured SWRC results, testifying the validity of the proposed model and indicating that the proposed model can satisfactorily account for the influence of soil volume change on its water retention property.

5 CONCLUSIONS

In order to analysis the difference between the conventional SWRC and $SWRC_{MIP}$ derived from PSD due to volume change, drying test was conducted on a reconstituted silty soil, together with the volume, suction and PSD measurements. The changes of the $SWRC_{MIP}$ families and their relation with conventional SWRC were analyzed. It can be concluded that deformation of the soil is the main reason for the difference between the conventional SWRC and $SWRC_{MIP}$.

A transformation model was proposed further. The model is based on the finding that the S_r-*s* (e=e_{min}) curve in S_r-*e*-*s* 3D surface, the S_{rMIP}-s (e=e_{min}) relationship in the S_{rMIP}-*e*-*s* 3D surface and the projection of the conventional SWRC on S_r (S_{rMIP})-o-*s* coordinate coincide at high suctions. This model takes the soil state with no longer volume change

as a reference, and takes the S_{rMIP}-s (e=e_{min}) curve as a reference curve in S_r-SWRC prediction, which connects the S_{rMIP}-e-s and S_r-e-s surfaces. The model is expected to be suitable for undisturbed and compacted–saturated samples undergoing drying path, no matter what stress histories they have before saturation.

ACKNOWLEDGEMENTS

The authors are grateful to the China Scholarship Council (CSC Grand No. 201406895026), Ecole des Ponts ParisTech, Shanghai Key Innovative Team of Cultural Heritage Conservation, the National Sciences Foundation of China (Grant No. 41572284, 41977214) and the Open Research Fund of State Key Laboratory of Geomechanics and Geotechnical Engineering, Institute of Rock and Soil Mechanics, Chinese Academy of Sciences (Grant No. Z013008) for the financial supports.

References

Aubertin M, Mbonimpa M, Bussière, B, et al. A model to predict the water retention curve from basic geotechnical properties. Canadian Geotechnical Journal, 2003; 40(6):1104-1122.

Aung K K, Rahardjo H, Leong E C, et al. Relationship between porosimetry measurement and soil-Water characteristic curve for an unsaturated residual soil. Geotechnical and Geological Engineering, 2001; 19(3):401-416.

Brooks RH, Corey AT. Hydraulic properties of porous media, *Colorado State University*, Fort Collins, CO, 1964; Hydrology Paper, (3): 27.

Delage P, Lefebvre G. Study of the structure of a sensitive Champlain clay and of its evolution during consolidation. Canadian Geotechnical Journal, 1984; 21(1):21-35.

Delage P, Audiguier M, Cui Y J, et al. Propriétés de rétention d'eau et microstructure de différents

géomatériaux. XIème Conférence Européenne de Mécanique des Sols et des Travaux de Fondations. 1995; 3:43-48.

Delage P, Audiguier M, Cui Y J, et al. Microstructure of a compacted silt. Canadian Geotechnical Journal, 1996; 33(1):150-158.

Delage P, Le T T, Tang A M, et al. Suction effects in deep Boom Clay block samples. Géotechnique, 2007; 57(2):239-244.

Della Vecchia G, Dieudonné Anne-Catherine, Jommi C, et al. Accounting for evolving pore size distribution in water retention models for compacted clays. International Journal for Numerical and Analytical Methods in Geomechanics, 2015; 39(7):702-723.

Feia S, Ghabezloo S, Bruchon J F, et al. Experimental evaluation of the pore-access size distribution of sands. Geotechnical Testing Journal, 2014; 37(4): 613-620.

Fiès J C, Bruand A. Particle packing and organization of the textural porosity in clay–silt–sand mixtures. European Journal of Soil Science, 1998; 49(4): 557-567.

Fredlund D G, Xing A. Equations for the soil-water characteristic curve. Canadian Geotechnical Journal, 1994; 31(4):521-532.

Fredlund D G. Role of the soil-water characteristic curve in unsaturated soil mechanics. The 7th International Conference on Unsaturated Soils UNSAT 2018. Editors: Charles W. W. Ng, Anthony K. Leung, Abraham C.F. Chiu & Chao Zhou. Blight Lecture. Hong Kong, 2018.

Gallipoli D, Wheeler S J, Karstunen M. Modelling the variation of degree of saturation in a deformable unsaturated soil. Géotechnique, 2003; 53(1):105-112.

Hu R, Chen Y F, Liu H H, et al. A water retention curve and unsaturated hydraulic conductivity model for deformable soils: Consideration of the change in pore-size distribution. Géotechnique, 2013; 63(16): 1389-1405.

Mašín D. Predicting the dependency of a degree of saturation on void ratio and suction using effective stress principle for unsaturated soils. International Journal for Numerical and Analytical Methods in Geomechanics, 2010; 34(1): 73-90.

579 Munoz-Castelblanco J A, Pereira J M, Delage P, et al. The water retention properties of a natural
580 unsaturated loess from northern France. Géotechnique, 2012; 62(2): 95-106.
581 Nuth M, Laloui L. Advances in modelling hysteretic water retention curve in deformable soils.
582 Computers and Geotechnics, 2008; 35(6):835-844.
583 Prapaharan S, Altschaeffl A G, Dempsey B J. Moisture Curve of Compacted Clay: Mercury Intrusion
584 Method. Journal of Geotechnical Engineering, 1985; 111(9):1139-1143.
585 Romero E, Gens A, Lloret A. Water permeability, water retention and microstructure of unsaturated
586 compacted Boom clay. Engineering Geology, 1999; 54(1-2):117-127.
587 Romero E, Della Vecchia G, Jommi C. An insight into the water retention properties of compacted
588 clayey soils. Géotechnique, 2011; 61(4): 313-328.
589 Simms P H, Yanful E K. Predicting soil-water characteristic curves of compacted plastic soils from
590 measured pore-size distributions. Géotechnique, 2002; 52(4):269-278.
591 Simms P H, Yanful E K. A pore-network model for hydromechanical coupling in unsaturated
592 compacted clayey soils. Canadian Geotechnical Journal, 2005; 42(2):499-514.
593 Sun D A, Sheng D C, Sloan S W. Elastoplastic modelling of hydraulic and stress–strain behaviour of
594 unsaturated soils. Mechanics of Materials, 2007; 39(3):212-221.
595 Sun W J, Cui Y J. Investigating the microstructure changes for silty soil during drying. Géotechnique,
596 2018; 68(4): 370-373.
597 Sun W J, Sun D A. Coupled modelling of hydro-mechanical behaviour of unsaturated compacted
598 expansive soils. International Journal for Numerical and Analytical Methods in Geomechanics,
599 2012; 36(8):1002-1022.
600 Sun W J, Sun D A, Fang L, et al. Soil-water characteristics of Gaomiaozi bentonite by vapour
601 equilibrium technique. Journal of Rock Mechanics and Geotechnical Engineering, 2014;
602 6(1):48-54.
603 Sun W J, Cui Y J, Hong Z S, et al. Moisture tension in fine-grained reconstituted soils at high initial
604 water contents. UNSAT-WASTE 2017, Shanghai, 2017: 131-138.

605 Tsiampousi A, Zdravkovic L, Potts D M. A three-dimensional hysteretic soil-water retention curve.
606 *Géotechnique*, 2013; 63(2): 155-164.
607 van Genuchten MT. A closed-form equation for predicting the hydraulic conductivity of unsaturated
608 soils. *Journal of Soil Science Society of America,* 1980; 44: 892-898.
609 Vaunat J, Casini F. A procedure for the direct determination of Bishop's χ parameter from changes
610 in pore size distribution. *Géotechnique*, 2017; 67(7): 631-636.
611 Wheeler S J. Inclusion of specific water volume within an elasto-plastic model for unsaturated soil.
612 *Canadian Geotechnical Journal*, 1996; 33(1): 42-57.
613 Zeng L L, Cui Y J, Conil N, et al. Experimental study on swelling behaviour and microstructure
614 changes of natural stiff Teguline clays upon wetting. Canadian Geotechnical Journal, 2017;
615 54(5): 700-709.
616

List of Tables

List of Figures

635 **List of Tables**

636 **Table 1. Indexes of samples drying to different target states**

637

No.	Sample	*s*(kPa)	*e*	*w*(%)	S_r(%)
	(1)-1	6	0.96	35.02	99.71
(1)	**(1)-2**	6	0.95	34.71	99.73
	(1)-3	5	0.98	35.70	99.28
	(2)-1	13	0.87	31.75	98.92
(2)	**(2)-2**	13	0.87	31.34	98.42
	(2)-3	13	0.87	31.68	98.58
	(3)-1	160	0.61	22.12	98.04
(3)	**(3)-2**	160	0.62	22.31	98.29
	(3)-3	160	0.62	22.31	98.24
	(4)-1	1000	0.54	14.29	71.42
(4)	**(4)-2**	1180	0.55	13.65	67.33
	(4)-3	870	0.55	14.44	71.92
	(5)-1	11020	0.51	7.58	40.61
(5)	**(5)-2**	10160	0.52	7.87	41.38
	(5)-3	20000	0.50	6.35	34.80
	(6)-1	65690	0.50	3.98	21.50
(6)	**(6)-2**	75610	0.51	4.07	21.70
	(6)-3	71510	0.50	4.24	22.89

638

639

640 **List of Figures**

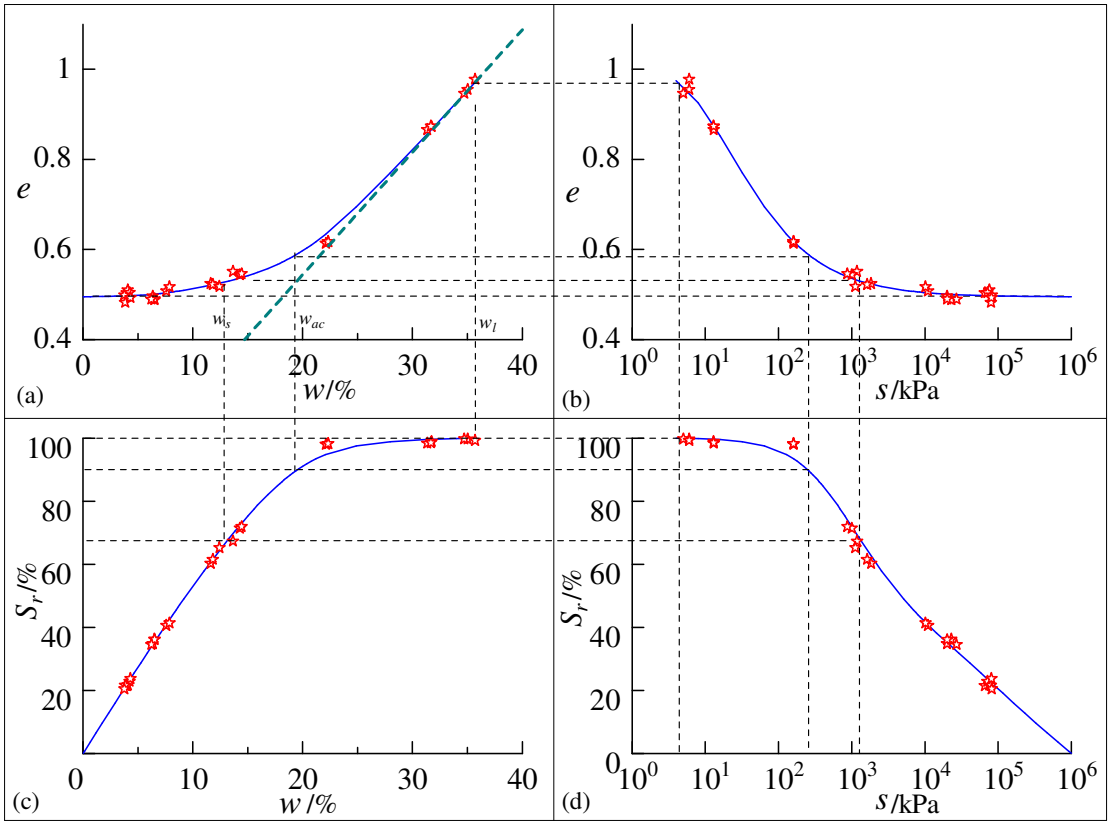

641

642 **Fig. 1** Results of the drying process of reconstituted Jossigny silt with $w_i = 1.5\ w_l$

643

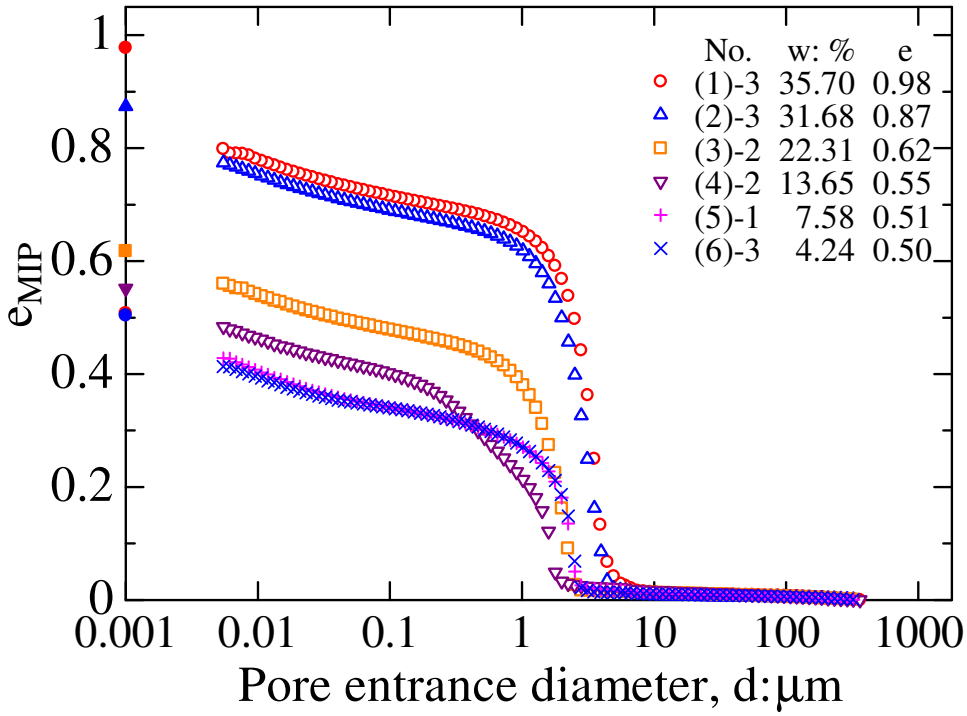

644

645 (a) Cumulative intrusion

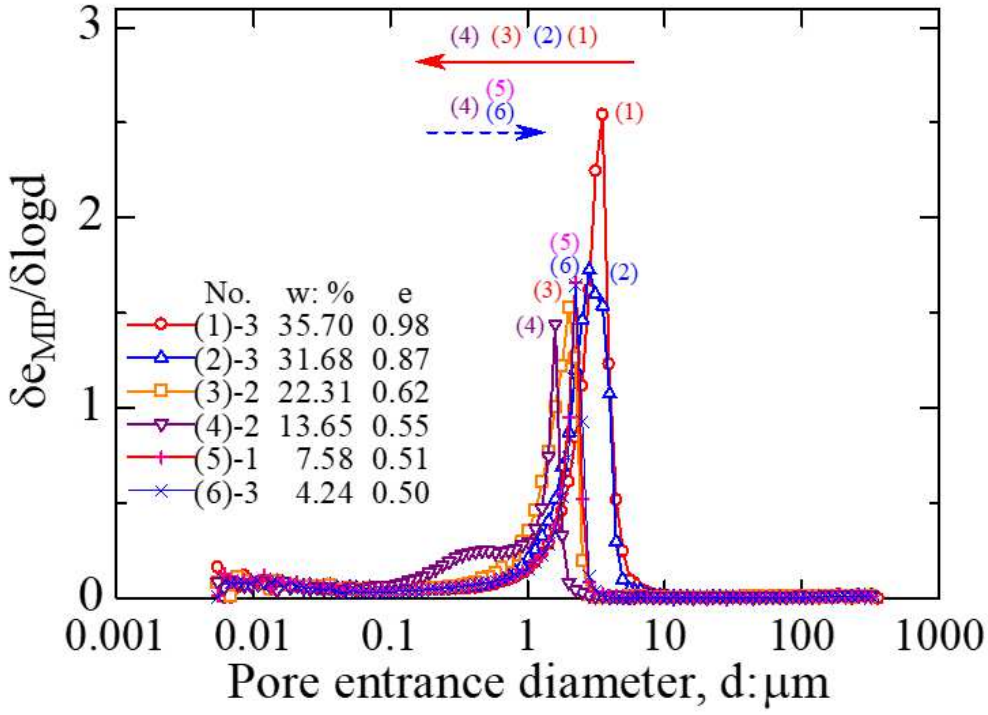

646

647 (b) PSD function

648 **Fig. 2** Pore size distribution of Jossigny silt during drying (data after Sun and Cui,

649 2018)

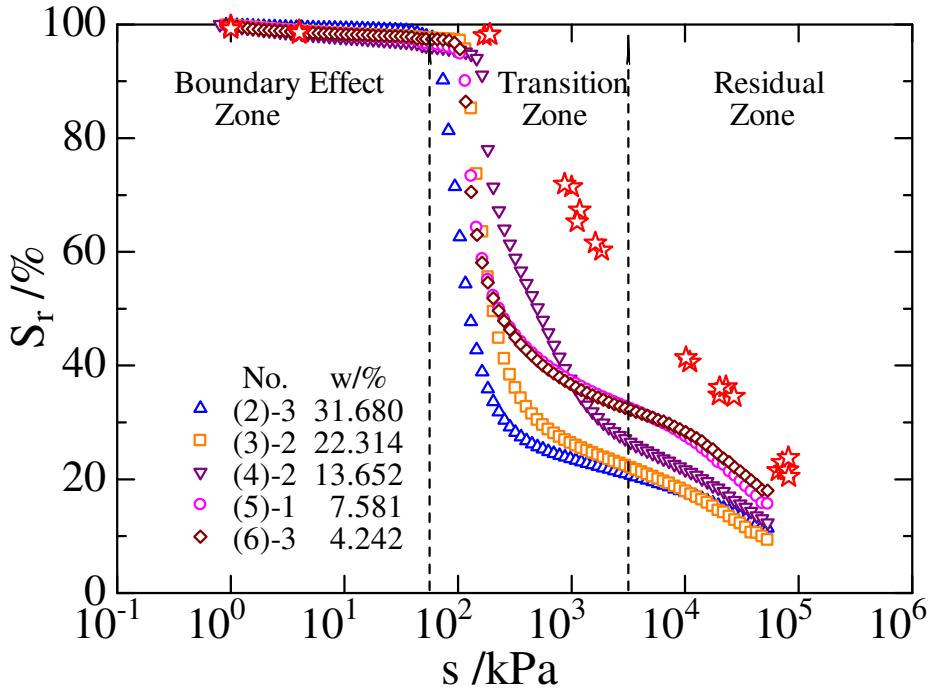

650

651 **Fig. 3** S_{rMIP}-s relationships and S_r-s relationship

652

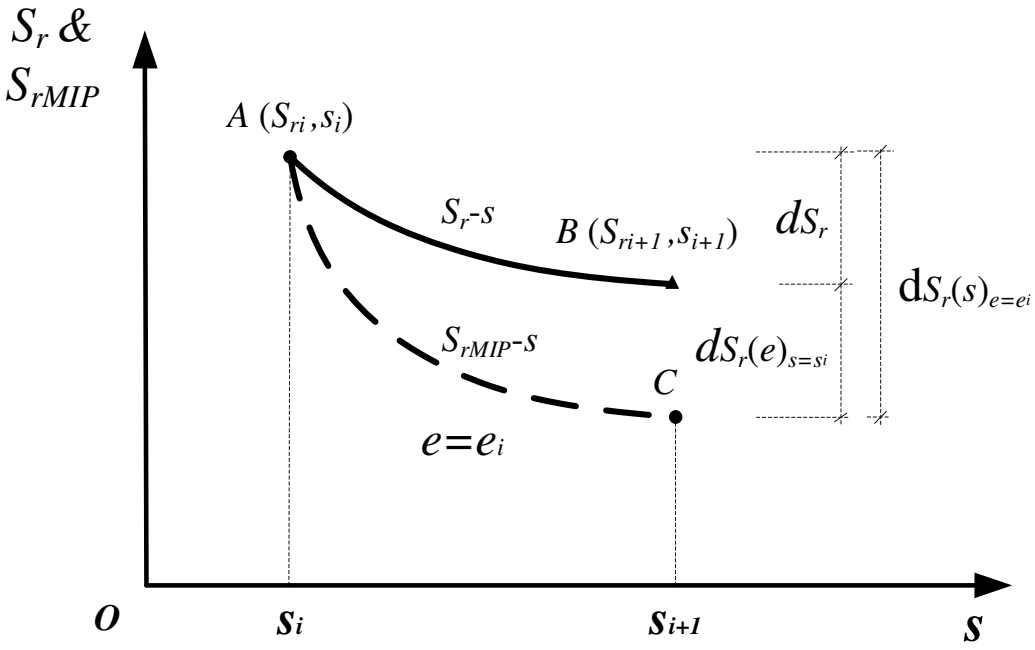

653

654 **Fig. 4** S_r (S_{rMIP}) - s relationship

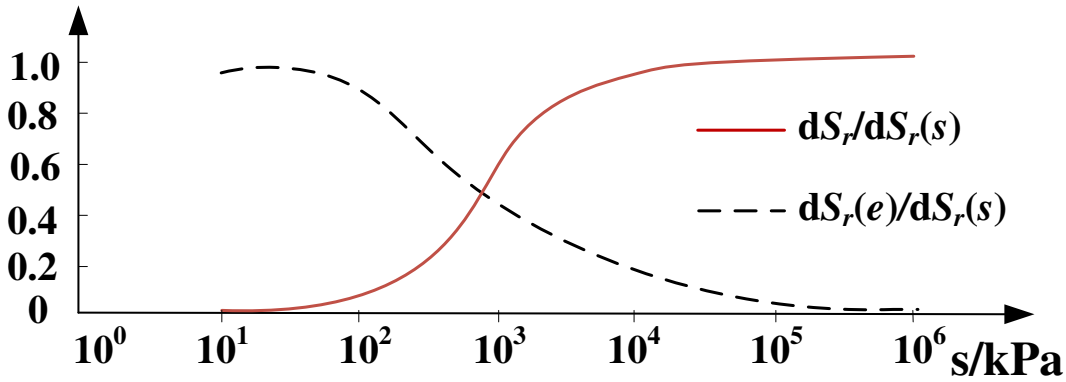

655

656 **Fig. 5** Changes of d$S_r(e)/dS_r(s)$ & $dS_r/dS_r(s)$ with suction

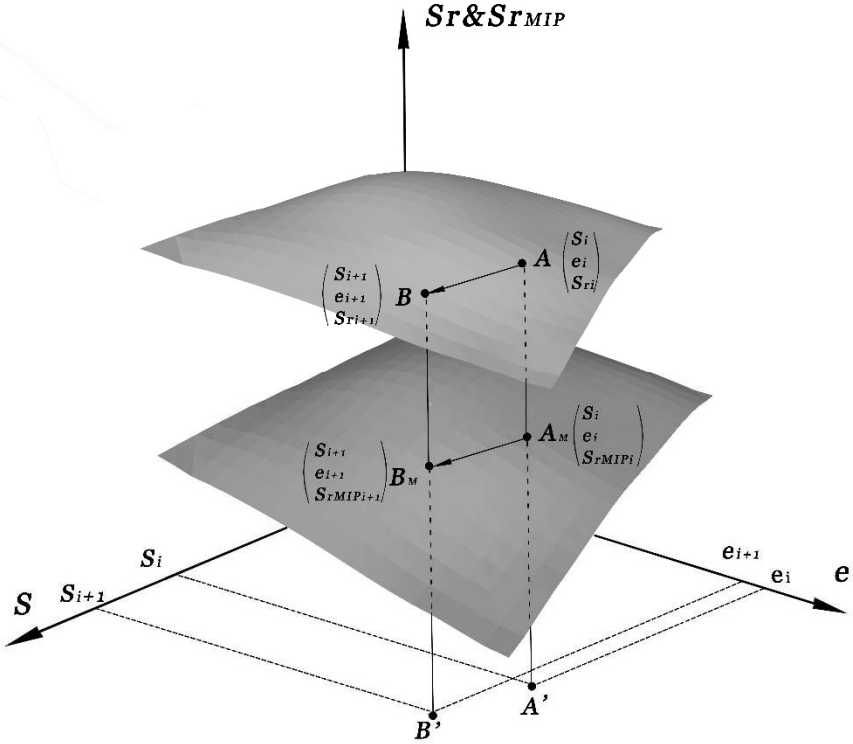

657

658 **Fig. 6** $S_r(S_{rMIP})$-*e*-*s* three-dimension diagram

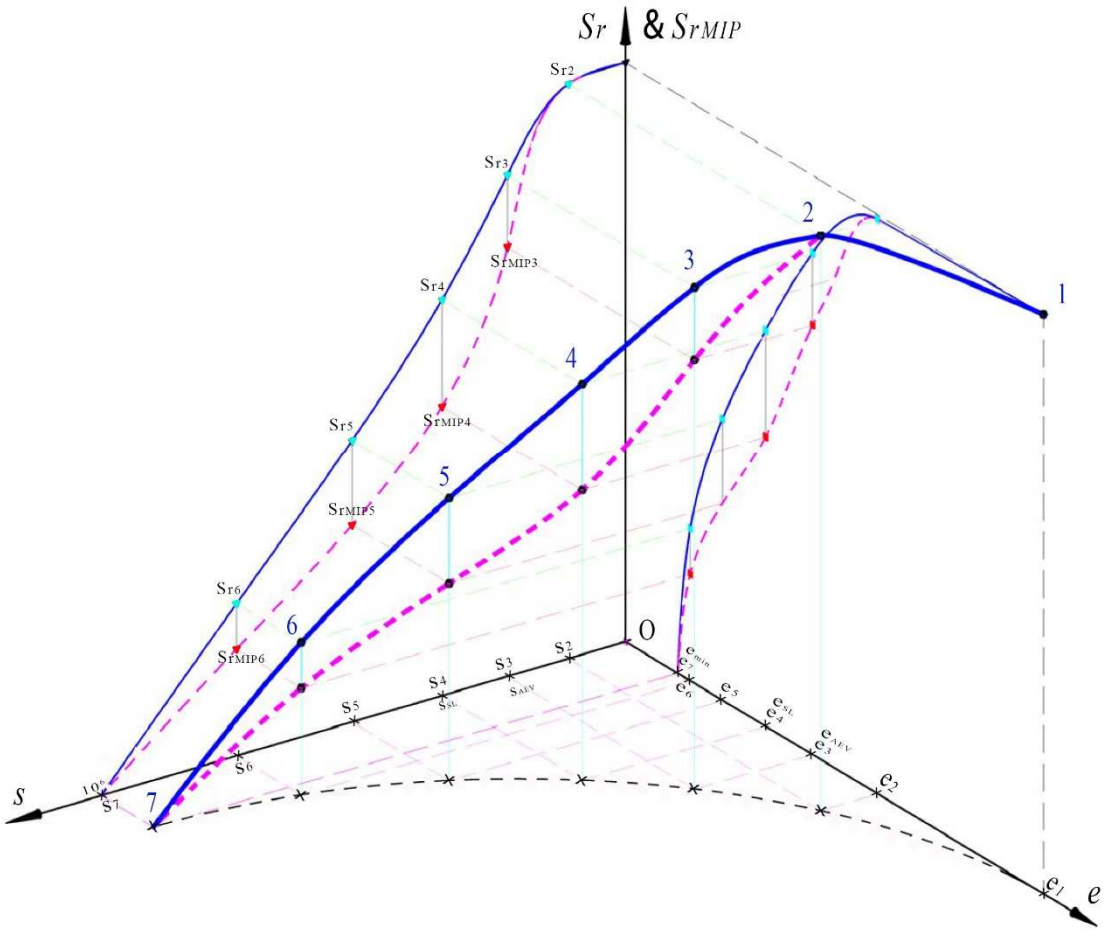

659

660 **Fig. 7** Projection of drying test results in S_r (S_{rMIP})-*e*-*s* three-dimension diagram

661

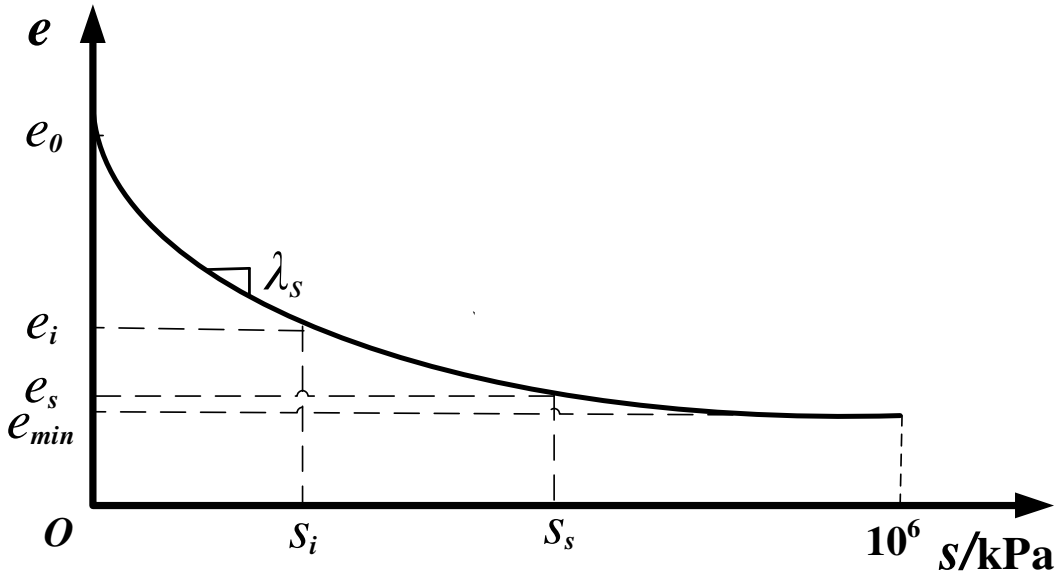

662

663 **Fig. 8** *e-s* relationship

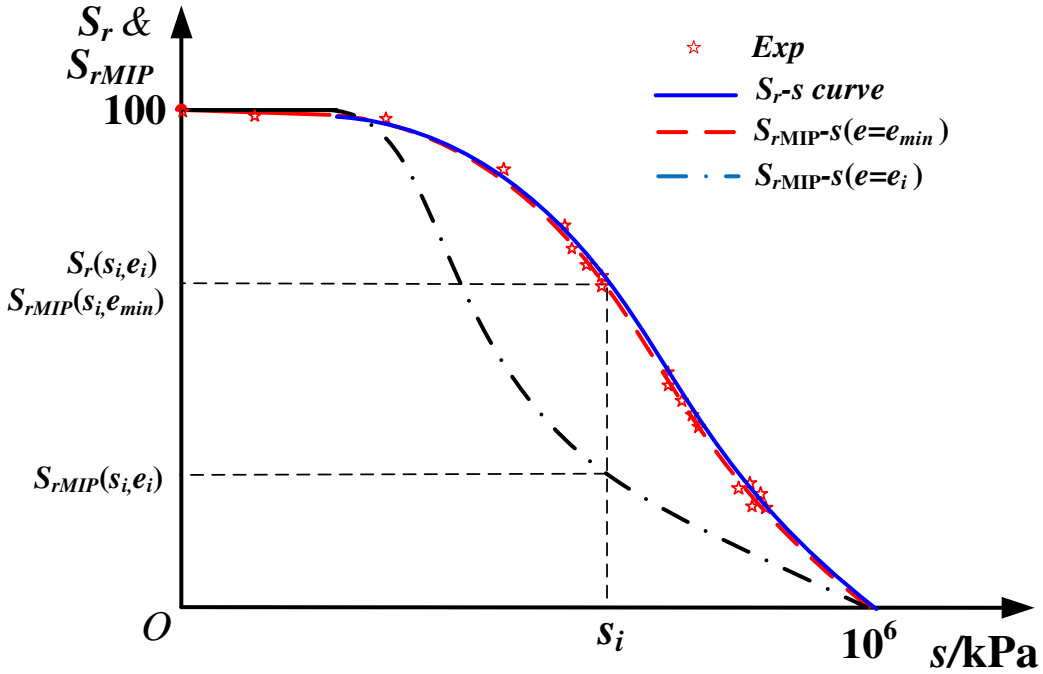

664

665 **Fig. 9** Comparison and connection between S_{rMIP}-*s* and S_r-*s* relationship

666

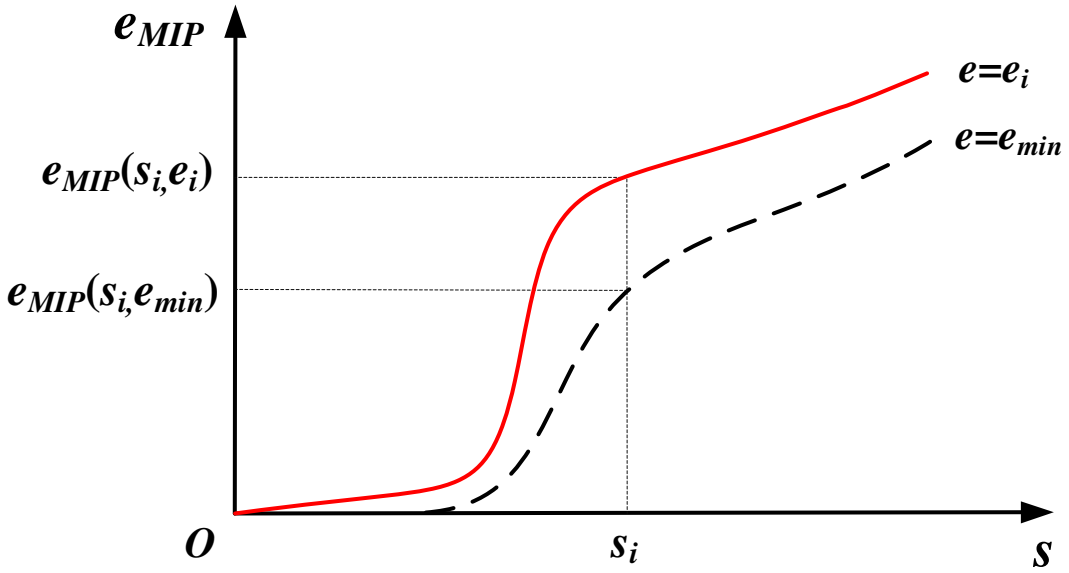

667

668 **Fig. 10** e_{MIP}-s relationship

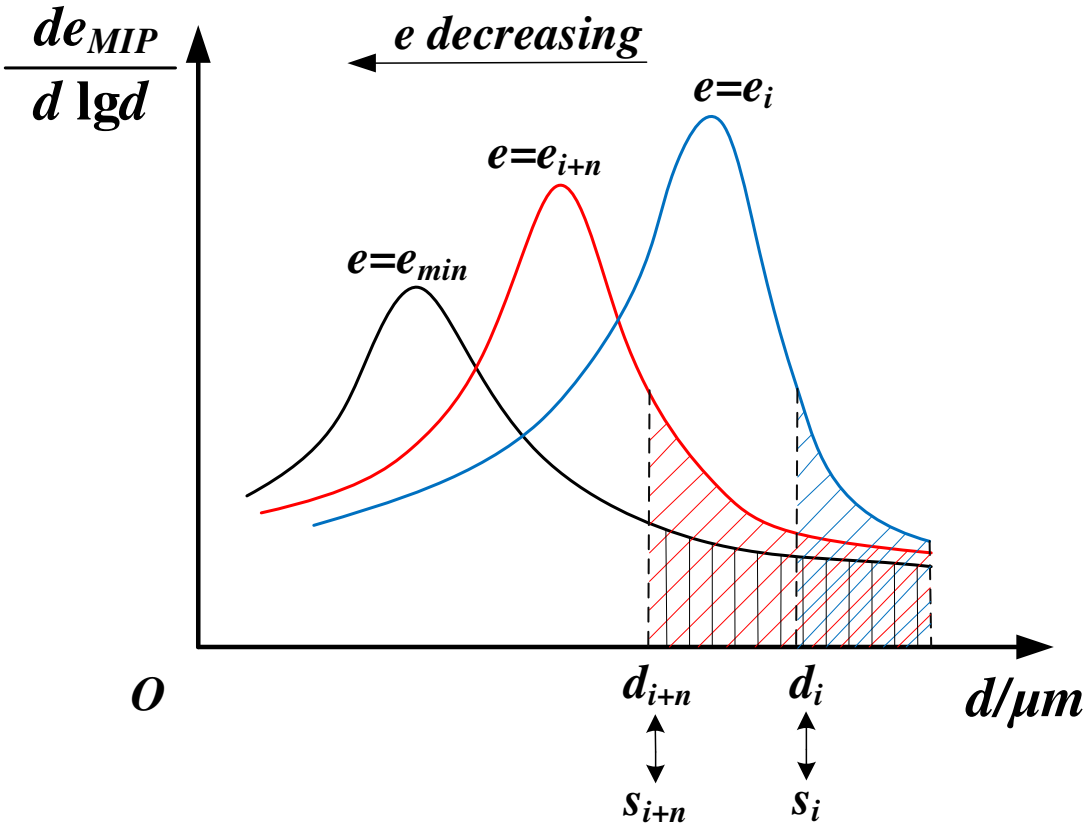

669

670 **Fig. 11** Change of PSD function with void ratio decreasing from $e=e_i$ to e_{min}

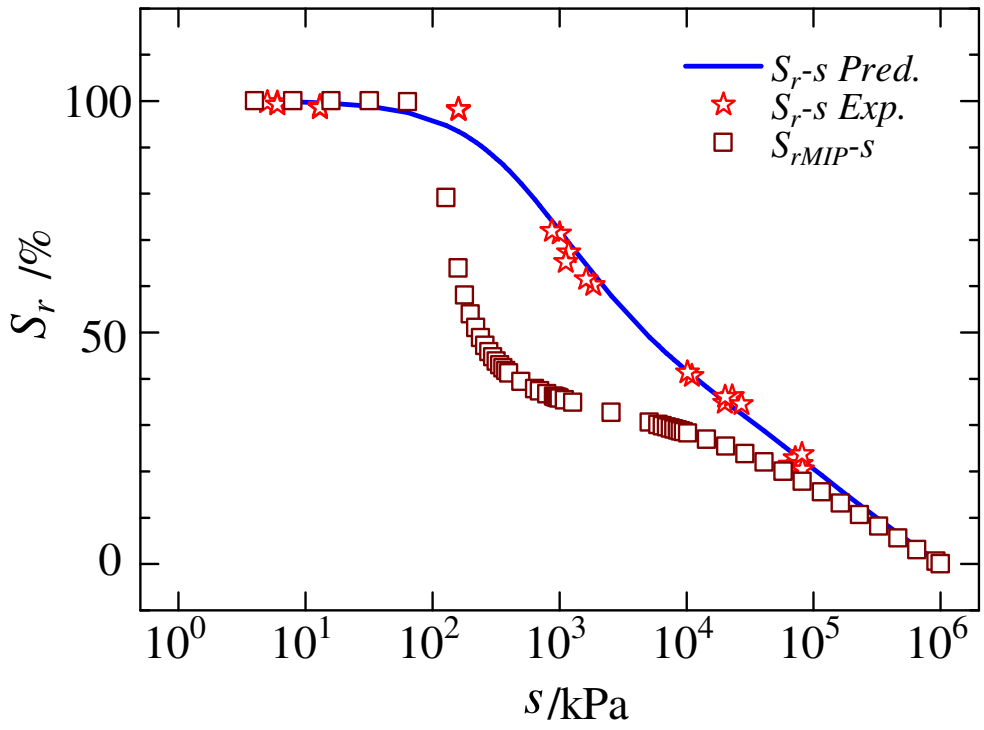

671

672 (a) S_r-s

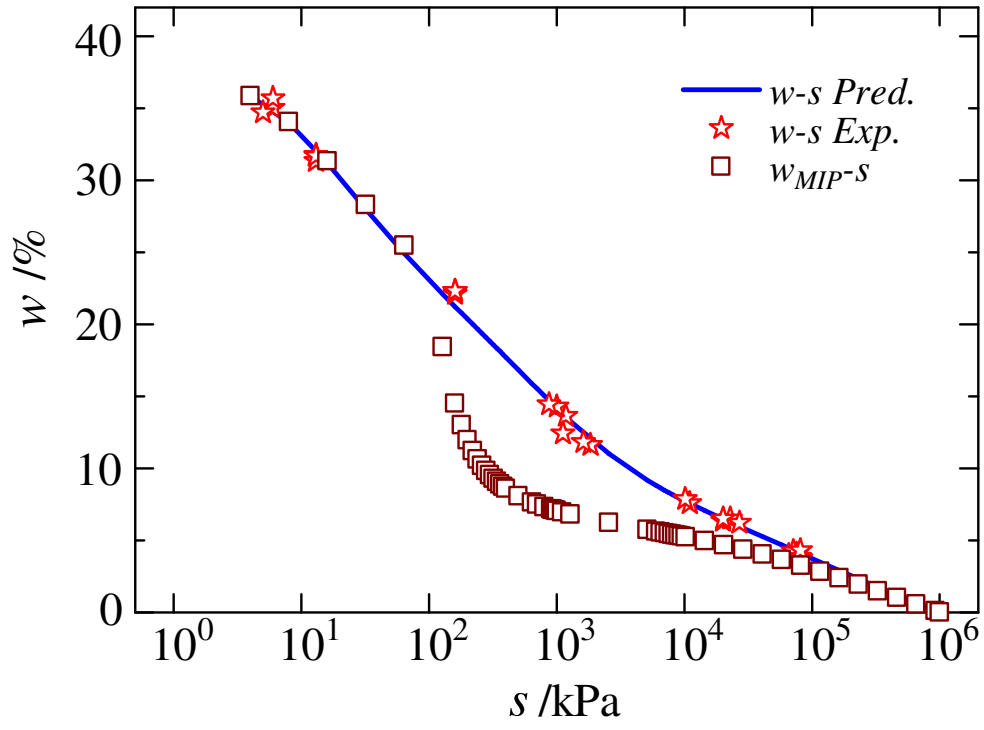

673

674 (b) w-s

675 **Fig. 12** Transformation of $SWRC_{MIP}$ to conventional SWRC in drying of reconstituted

676 Jossigny silt